First Insights into the Applicability and Importance of Different 3D Magnetic Field Extrapolation Approaches for Studying the Preeruptive Conditions of Solar Active Regions

Marianna B. Korsós[1,2,3] ◦, Robert Jarolim[4] ◦, Robertus Erdélyi[2,3,5] ◦, Astrid M. Veronig[4,6] ◦, Huw Morgan[7] ◦, and Francesca Zuccarello[1,8] ◦

[1] Dipartimento di Fisica e Astronomia "Ettore Majorana," Università di Catania, Via S. Sofia 78, I-95123 Catania, Italy
[2] Department of Astronomy, Eötvös Loránd University, Pázmány Péter sétány 1/A, H-1112 Budapest, Hungary
[3] Hungarian Solar Physics Foundation, Petőfi tér 3, H-5700 Gyula, Hungary
[4] Universität Graz, Institute of Physics, Universitätsplatz 5, A-8010 Graz, Austria
[5] Solar Physics & Space Plasma Research Center (SP2RC), School of Mathematics and Statistics University of Sheffield, Hounsfield Road, Sheffield S3 7RH, UK
[6] Universität Graz, Kanzelhöhe Observatory for Solar and Environmental Research, Kanzelhöhe 19, A-9521 Treffen am Ossiacher See, Austria
[7] Adran Ffiseg, Prifysgol Aberystwyth, Ceredigion, Cymru, SY23 3BZ, UK
[8] INAF—Catania Astrophysical Observatory, Via S. Sofia 78, I-95123 Catania, Italy.

Abstract

The three-dimensional (3D) coronal magnetic field has not yet been directly observed. However, for a better understanding and prediction of magnetically driven solar eruptions, 3D models of solar active regions are required. This work aims to provide insight into the significance of different extrapolation models for analyzing the preeruptive conditions of active regions with morphological parameters in 3D. Here, we employed potential field (PF), linear force-free field (LFFF), and nonlinear force-free field (NLFFF) models and a neural network-based method integrating observational data and NLFFF physics (NF2). The 3D coronal magnetic field structure of a "flaring" (AR11166) and "flare-quiet" (AR12645) active region, in terms of their flare productivity, is constructed via the four extrapolation methods. To analyze the evolution of the field, six prediction parameters were employed throughout, from the photosphere up to the base of the lower corona. First, we find that the evolution of the adopted morphological parameters exhibits similarity across the investigated time period when considering the four types of extrapolations. Second, all the parameters exhibited preeruptive conditions not only at the photosphere but also at higher altitudes in the case of active region (AR) 11166, while three out of the six proxies also exhibited preeruptive conditions in the case of AR12645. We conclude that: (i) the combined application of several different precursor parameters is important in the lower solar atmosphere to improve eruption predictions, and (ii) to gain a quick yet reliable insight into the preflare evolution of active regions in 3D, the PF and LFFF are acceptable; however, the NF2 method is likely the more suitable option.

1. Introduction

The different magnetic configurations of solar active regions can lead to different dynamic behavior. For example, active regions with a γ- and/or δ-spot configuration(s) have the most magnetically complex structure and can store a huge amount of free magnetic energy that is responsible for the most powerful solar events, like flares and coronal mass ejections (CMEs; e.g., Sammis et al. 2000; Georgoulis et al. 2019; Toriumi & Wang 2019).

Magnetic free energy can accumulate in at least two ways: e.g., through the emergence of magnetic flux from the solar interior to the solar atmosphere, or by the twisting and shearing of the magnetic field due to footpoint motions of an active region in the photosphere (Fletcher et al. 2011; van Driel-Gesztelyi & Green 2015). Liokati et al. (2022) found that, when the stored magnetic free energy is above 2×10^{32} erg, then an active region is likely to erupt. However, the presence of free magnetic energy in an active region does not guarantee the occurrence of a large solar eruption, since the release of the free energy may not happen all at once (Wiegelmann et al. 2014; Green et al. 2018).

The challenge of predicting solar eruptions benefits from the analysis of extracted parameters, usually from photospheric line-of-sight (LOS) or vector magnetograms. These scalar parameters, reduced from a whole active region, can be calculated by a variety of techniques (e.g., thresholding, feature recognition, etc.) and applied for eruption prediction purposes (see, e.g., Barnes et al. 2016; Korsós & Erdélyi 2016; Florios et al. 2018; Korsós et al. 2018; Leka et al. 2019; Korsós et al. 2020; Georgoulis et al. 2021, and references therein). Some recent pioneering approaches attempt to incorporate extreme ultraviolet data and use machine learning in order to improve forecasting accuracy (see, e.g., Kim et al. 2019; Leka et al. 2023; Sun et al. 2023), but there are caveats, as pointed out in Liu & Huang (2021).

Detailed information on measuring, and the consequent modeling, of the 3D magnetic field structure of an active region would be important to obtain a more accurate insight into the preeruptive conditions in the solar atmosphere. Direct observations
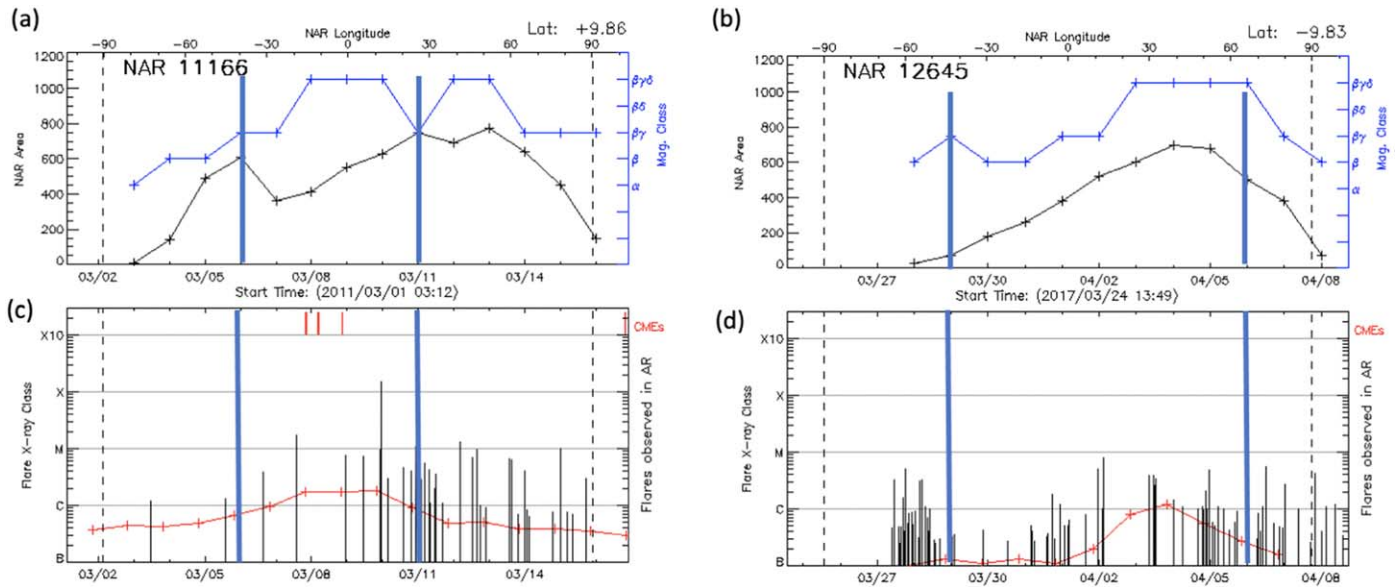
Figure 1. Panels (a) and (b) show the area evolution of AR11166 and AR12645, respectively. The longitude of the active regions is shown at the top of the corresponding plots. The vertical dashed lines mark when the active regions cross the east and west limbs. Panels (c) and (d) display the peak time and size of the soft X-ray flares that have occurred in the host active regions (vertical black lines). The soft X-ray background is shown in red. The times of halo CME events (width >135°) that occurred during the period are visualized as red bars at the top of the panels. In panels (a)–(d), the long blue vertical lines represent the investigation period of the two active regions during this work. Credits to HELIO (http://helio.mssl.ucl.ac.uk).

of the 3D magnetic field in the lower solar corona are currently only possible for exceptional observing conditions and under certain special circumstances (e.g., Kuridze et al. 2019). Instead, the measured LOS component or the full vector magnetic fields observed at the photosphere can be used as a lower boundary to model the atmospheric magnetic field using potential field (PF), linear force-free field (LFFF), or more complex nonlinear force-free field (NLFFF) extrapolation models (Wiegelmann & Sakurai 2021). Consequently, without improved observational constraints (Erdélyi et al. 2022), static extrapolation models currently remain our best practical approach for approximating active region magnetic field structures.

Korsós et al. (2018) found that the prediction of major solar eruptions, such as flares, can be improved by incorporating data from the lower solar atmosphere (LSA), which extends from the photosphere to approximately 4 Mm above the solar surface. Korsós et al. (2020) and Korsós et al. (2022) noted that using PF extrapolation data allows for earlier identification of the preflare evolution phase of predictor parameters, particularly in the region above the photosphere within the LSA (up to 2 Mm). The PF offers a simplified yet insightful representation of the 3D magnetic field topology of an active region at a given moment of time, capturing the essential large-scale structure without the complexities of currents and their dynamics. While the PF approach is applicable for studying the topology and preflare evolution of the 3D magnetic field of an active region through morphological parameters, more detailed and accurate modeling, including currents, is often necessary for further comprehensive analysis.

Applying a PF extrapolation gives an overall view of an active region and would not be suitable, of course, to estimate the available free magnetic energy itself. Using the PF to model the vertical z direction does not imply that the photospheric motion at the lower boundary is force free. This is because, at each time step, the lower boundary is considered separately when constructing the active region magnetic structure. Thus, the PF approximation, despite its simplicity, can still offer

valuable insights into a complex system, though its limitations must be considered. Therefore, we emphasize again that a simple PF model cannot be used to diagnose the flare energy or dynamics. However, in practice, applying certain precursors in the LSA based on the PF approximation can improve lead time and can also give an approximate indication of flare strength (Korsós et al. 2020, 2022).

In this study, we extract and analyze selected prediction parameters based on the recommendations and findings of Florios et al. (2018) and Georgoulis et al. (2021), not only at the photosphere but in the entire LSA. To test the idea, this current examination is conducted for two representative active regions exhibiting δ-spot configurations but with distinctly different flaring activities. Our objective is to better understand the significance of various 3D extrapolation approaches and their impact on future flare prediction using different morphological parameters in the LSA.

The work is structured as follows: Section 2 introduces the selected two active regions. Section 3 describes the adopted tools for analyzing the 3D magnetic field structure of the two active regions. In Section 4, we present the results. Key findings and conclusions, along with a suggestion of future work, are given in Section 5.

2. The Selected "Flaring" and "Flare-quiet" Solar Active Regions

NOAA active region (AR) 11166 ("flaring") and NOAA AR12645 ("flare-quiet") were chosen to investigate the level of importance of the four different 3D extrapolation approaches for the following reasons.

1. Both of the active regions have complex δ-spot magnetic configurations (see Figures 1(a)–(b)).
2. Both were between E60 to W60 for a suitably long period of time (see Figures 1(a)–(b)).
3. However, they exhibit distinctly different histories of flare activity (see Figures 1(c)–(d)). In the case of
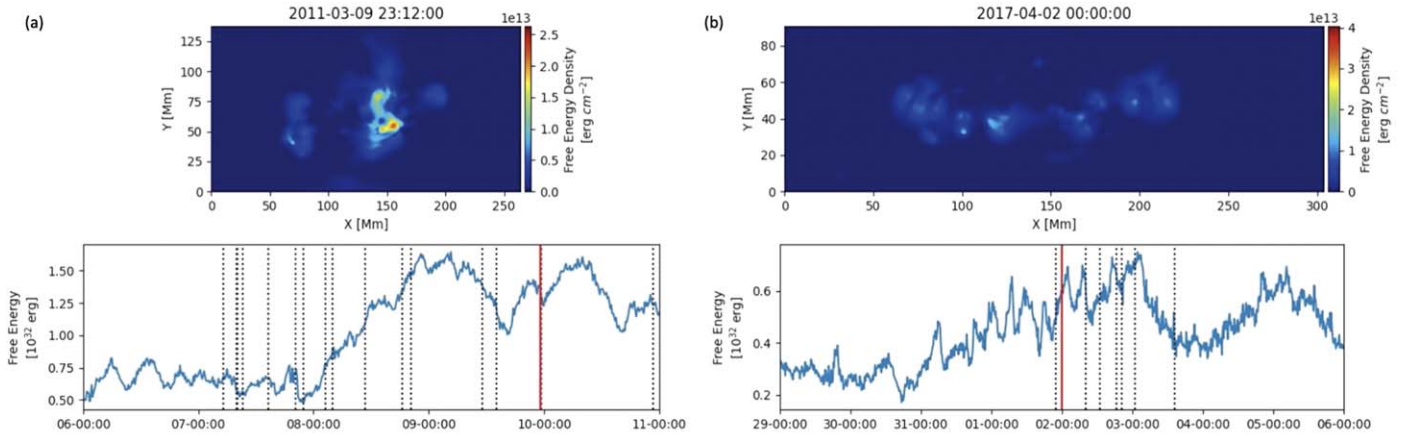
Figure 2. This figure presents a snapshot from a 1 minute and 36 s animation available in the online version. The upper panels depict the two-dimensional free energy density maps of (a) AR11166, representing a flaring active region, at 23:12 on 2011 March 9, around the time of the X1.5 flare, and (b) AR12645, representing a nonflaring active region, at 00:00 on 2017 April 2. The color bars indicate the magnitude of the free energy density. The lower panels for (a) and (b) illustrate the evolution of the estimated stored magnetic free energy for AR11166 and AR12645, respectively. Two red vertical lines indicate the position of the animation slider. In the cases of both active regions, black vertical dashed lines signify the flares they hosted, as detailed in Figures 1(c)–(d). Additionally, in the animation, a red vertical dashed line marks the X1.5 flare on the panel depicting the evolution of free energy in AR11166. In that snapshot, the slider overlays this vertical dashed line as this snapshot was taken around the X1.5 flare.

(An animation of this figure is available.)

AR11166, the studied X1.5 flare event occurred on 2011 March 9 at 23:13 UTC and was located in the northwest (N23°W11°) part of the solar disk. In contrast, AR12645 produced no intense flares during its transit.

In this work, we investigate how some of the morphological parameters evolve using various sets of extrapolation data (i.e., PF and various nonlinear force-free approaches). Our goal is to ascertain a more suitable (e.g., practical and cost-effective) extrapolation method(s) for future statistical studies. This may help to enhance our understanding of how the predictive capabilities of combined predictors can be improved through the application of a 3D magnetic field extrapolation model in the LSA.

3. Data Processing

To determine the 3D magnetic field structures of AR11166 and AR12645 (see, e.g., Figures 2(a)–(b)), we utilized the following four extrapolation models, which rely on observations of their respective photospheric vector magnetic fields:

1. The PF, LFFF, and NLFFF extrapolation models of Wiegelmann et al. (2012).
2. The physics-based neural network (Raissi et al. 2019) method, which integrates both observational data and the physical NLFFF model of Jarolim et al. (2023), called NF2.

The photospheric vector magnetic fields of AR11166 and AR12645 consist of the B_r, B_t, and B_p components, obtained from the Spaceweather Helioseismic Magnetic Imager Active Region Patches (SHARP)[9] catalog for the duration of the investigated time intervals, as indicated by the pair of blue vertical lines in Figure 1. We constructed the extrapolated magnetogram data from the $z = 0$ level (representing the photosphere) up to 3.6 Mm in the LSA with a 60-minute cadence using the models by Wiegelmann & Sakurai (2021) and Jarolim et al. (2023). The step size in the vertical direction

used is $z = 0.36$ Mm, which matches the SHARP pixel size. Furthermore, for the LFFF extrapolation, the already calculated and stored total twist parameter α in the fits-header of the SHARP data series was used. We note that the procedures to create the SHARP database can introduce additional errors (e.g., azimuth disambiguation; Bobra et al. 2014), which can further affect subsequent magnetic field extrapolations.

For both active regions, the evolution of the free magnetic energy (E_{free}) is estimated, as a next step. E_{free} represents the excess energy of a magnetic configuration compared to its minimum-energy (i.e., potential) state:

$$E_{\text{free}} = E_{\text{FF}} - E_{\text{PF}} = \int_V \left(\frac{B_{\text{FF}}^2}{8\pi} - \frac{B_{\text{PF}}^2}{8\pi} \right) dV, \quad (1)$$

where B_{FF} and B_{PF} refer to the force-free and PF solution, respectively. Investigating the available free energy in a magnetic configuration is crucial since a portion of this stored energy can be released during a flaring process. The actual spatial and temporal variation of the calculated E_{free} for the two active regions is displayed in Figures 2(a)–(b), respectively. The upper panels of Figure 2 show the free energy density map of (a) AR11166 on 2011 March 9 23:12, and (b) AR12645 on 2017 April 2 00:00. The free magnetic energy density maps are derived by computing the energy difference per grid cell and integrating along the vertical axis. Based on Figure 2(a), the largest free energy is present where the X1.5 flare actually occurred (the location of the X1.5 flare can be seen in Figure 1 of Vemareddy & Wiegelmann 2014).

Based on the lower panel of Figure 2(a), the E_{free} of AR11166 increased from approximately 0.5–1.5 $\times 10^{32}$ erg in just one day. However, in the lower panel of Figure 2(b), the E_{free} of AR12645 grew from around 0.3 to only 0.7 $\times 10^{32}$ erg, taking a little more than three days. In both active regions, E_{free} increased during their emerging phases. Based on the E_{free} evolution of the two active regions, it can now be concluded that AR11166 possessed approximately one order of magnitude more available free magnetic energy than AR12645. Nevertheless, it is noteworthy

_____
9 http://jsoc.stanford.edu/doc/data/hmi/sharp/sharp.htm

Table 1
Summary of the Applied Proxy Parameters and Their Results Based on PF, LFFF, NLFFF, and NF2 Coronal Field Extrapolations

		AR11166				AR12645			
	Threshold								
Free magnetic energy, E_{free} (Liokati et al. 2022)	2^*10^32 (erg)	Yes				n/a			
Proxy parameters		Atmospheric height range (Mm)				Atmospheric height range (Mm)			
Based on FLARECAST project		PF	LFFF	NLFFF	NF2	PF	LFFF	NLFFF	NF2
Main polarity inversion line, MPIL (Falconer et al. 2003)	62 (Mm)	0–1.08	0–1.08	0–3.6	0–3.6	0–1.8	0–1.8	0–3.6	0–3.6
Unsigned magnetic flux of the PIL, $logR$ (Schrijver 2007)	5	0	0	0–0.72	0–0.72	n/a	n/a	n/a	n/a
Effective connected magnetic field, B_{eff} (Georgoulis & Rust 2007)	750 [G]	0–0.36	0–0.36	0–1.44	0–1.8	n/a	n/a	n/a	n/a
Gradient-weighted length of strong-field PILs, WL_{SG} (Falconer et al. 2012)	10^4 [G]	0–2.16	0–2.16	0–3.6	0–3.6	0–2.52	0–2.52	0–3.6	0–3.6
Ising energy, E_{Ising} (Ahmed et al. 2010)	10^4 [1/pixels]	0–3.6	0–3.6	0–3.6	0–3.6	0–3.6	0–3.6	0–3.6	0–3.6
Oscillatory behavior of magnetic helicity fluxes (Korsós et al. 2022)	Common period	0–2.16	0–2.16	0–1.8	0–1.8	n/a	n/a	n/a	n/a

Notes. The first column presents the name of the parameter, and the second column details their own threshold values. The last eight columns indicate the height range where each of the investigated parameters fulfill their respective preeruptive conditions in the case of AR11166 and AR12645, respectively. "N/a" means that the parameter does not exceed its own threshold value.

that the available E_{free} of AR11166 was below the 2×10^{32} erg threshold level, as suggested by Liokati et al. (2022) for larger solar eruptions, a day before the occurrence of the X1.5 flare.

However, the presence of a large amount of E_{free} in an active region does not necessarily guarantee the occurrence of a large solar eruption, as the release of that free energy may occur at different, successive times. To further analyze the eruption capabilities of the two different active regions, we examined the evolution of various proxy parameters as a function of height. In particular, six morphological parameters (see Table 1) were selected because they are widely used and are very promising predictors in solar flare prediction schemes, as concluded by the FLARECAST project (Georgoulis et al. 2021). These proxies were derived from the extrapolated magnetic field data. The codes used for calculating the six proxies (see Sections 4.2–4.6) were obtained from the algorithm repository of the FLAR-ECAST project.[10] Finally, the time series of derived parameters were thoroughly investigated and analyzed as a function of height in the LSA.

4. Morphological Parameters

4.1. Main Polarity Inversion Line

The polarity inversion line (PIL) separates patches of positive and negative fluxes, where the gradient of the magnetic field is large and indicative of a strong shearing or twisting of the magnetic field structure of an active region. This type of magnetic field configuration also very often is the source of large flare and CME eruptions.

---

[10] https://dev.flarecast.eu/stash/projects

The main PIL (MPIL) separates the major polarity regions of an active region. Falconer et al. (2003) studied the CME predictability of the measured MPIL, while Mason & Hoeksema (2010) found that it could also be used for flare prediction purposes. They suggested that a large solar eruption could be anticipated within a two-day period if the MPIL exceeds the threshold of 62 Mm, where the observed transverse field strength is greater than 150 Gauss. Therefore, here, we investigated when the MPIL reached a threshold level of 62 Mm at different atmospheric heights (see Figure 3 and Table 2).

1. *AR11166.* In the case of PF and LFFF, the MPIL starts to increase about 2.5 days before the X1.5 flare between 0 and 1.8 Mm (Table 2). Above a height of 1.8 Mm, no clear evolution pattern(s) is seen in the time series of the MPIL, like for the lower atmospheric heights. Meanwhile, the same duration of ∼2.5 days of the increasing phase of the MPIL can be identified throughout the investigated atmospheric heights by the NLFFF and NF2 data before the X1.5 flare eruption. The MPIL reached the 62 Mm threshold about two days before the X1.5 flare between 0 and 1.08 Mm in the case of both PF and LFFF data (see Table 2). However, above 1.08 Mm, the MPIL remained less than 62 Mm. On the other hand, in the case of the NLFFF and NF2 approaches, the MPIL grew above the threshold level at all investigated atmospheric heights. For NLFFF, the MPIL became larger than 62 Mm approximately two days earlier between 0 and 2.16 Mm, and at higher altitudes, it occurred around 1.5 days earlier. According to the NF2 extrapolation, the 62 Mm threshold was reached about two days earlier before the X1.5 flare
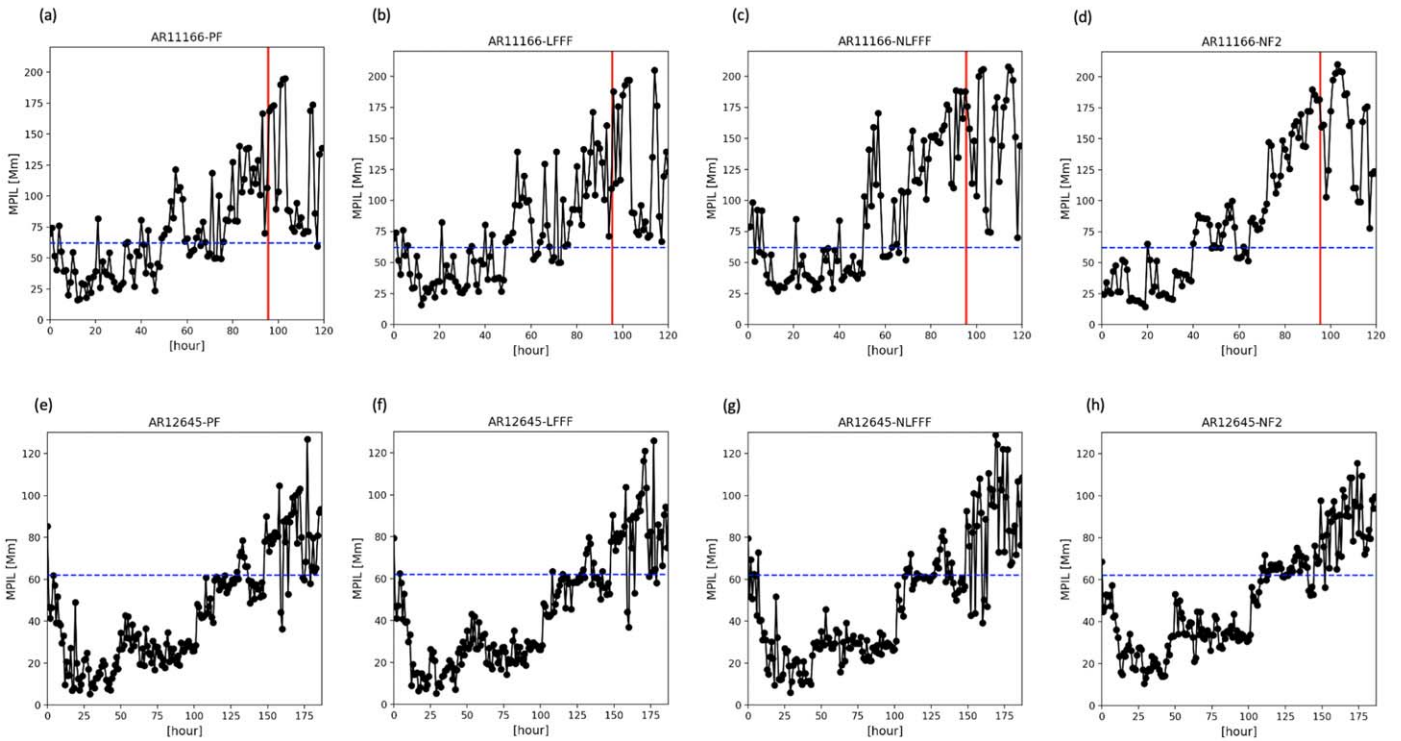
Figure 3. Panels (a)–(d) refer to the evolution of the MPIL parameter at 0.36 Mm above the solar surface based on the PF, LFFF, NLFFF, and NF2 extrapolation schemes, respectively, in the case of AR11166. The red vertical lines represent the onset time of the X1.5 flare. Panels (e)–(h) are the same as the top row but for AR12645. The blue horizontal lines represent the threshold value of the MPIL (see Table 1).

Table 2
Summary of MPIL Analysis for AR11166 and AR12645 Using PF, LFFF, NLFFF, and NF2 Extrapolation Schemes

Height (Mm)	$T_{MPIL} > 62M$ (hr)				MPIL (Mm) at the Reference Time			
	PF	LFFF	NLFFF	NF2	PF	LFFF	NLFFF	NF2
				AR11166				
0	51	50	46	54	179.9	193.3	181.6	163.2
0.36	49	49	45	56	168.6	187.6	175.9	159.3
0.72	50	51	45	45	89.7	91.5	152.7	124.1
1.08	54	53	44	45	64.0	73.4	125.3	123.1
1.44	...	...	45	33	59.4	59.4	123.7	125.8
1.8	...	...	54	33	57.6	60.2	121.7	171.9
2.16	...	...	56	34	34.3	34.2	113.6	170.2
2.52	...	...	37	35	33.2	33.2	118.5	168.5
2.88	...	...	29	34	22.8	31.7	190.3	166.1
3.24	...	...	39	34	15.2	16.7	103.8	125.1
3.6	...	...	39	34	15.3	18.4	84.4	115.7
				AR12645				
0	71	71	71	75	137.2	139.6	142.4	140.3
0.36	59	59	72	74	93.4	93.5	108.5	95.5
0.72	38	38	54	51	89.0	88.9	79.1	89.0
1.08	39	35	38	40	85.9	85.6	95.7	86.9
1.44	20	35	38	37	83.5	83.1	71.5	72.5
1.8	6	6	36	37	80.8	90.3	71.2	71.9
2.16	...	...	39	10	60.0	59.5	70.9	66.8
2.52	...	...	38	7	58.0	57.7	72.3	67.2
2.88	...	...	4	3	56.2	55.9	72.6	66.8
3.24	...	...	5	2	53.2	52.4	72.8	66.4
3.6	...	...	4	2	47.0	52.3	73.5	66.2

Notes. The first column presents the investigated heights, and the following four columns detail how many hours earlier the MPIL exceeded the 62 Mm threshold level at various atmospheric heights based on the four extrapolation datasets. The last four columns display the actual values of the MPIL at the reference time. For AR11166, the reference time corresponds to the occurrence of the X1.5 flare, while for the nonflaring active region AR12645, the reference time is the final data point of the time series.
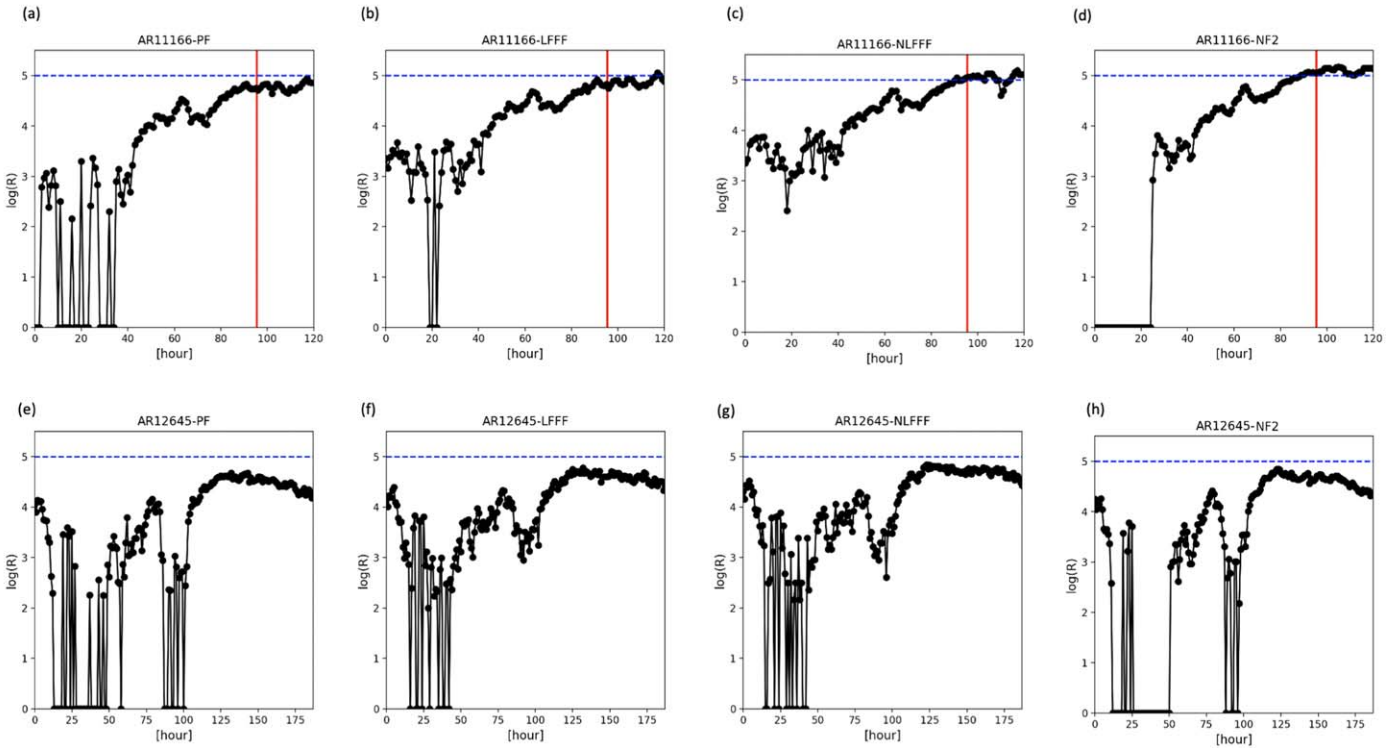
Figure 4. Panels (a)–(d) refer to the evolution of the log R parameter at a height of 0.36 Mm above the solar surface based on the PF, LFFF, NLFFF, and NF2 extrapolations, respectively, in the case of AR11166. The red vertical lines represent the onset time of the X1.5 flare. Panels (e)–(h) refer to the case of nonflaring AR12645.

between 0 and 1.08 Mm, while above 1.08 Mm, it happened approximately 1.5 days earlier.

2. *AR12645.* Based on PF and LFFF extrapolations, the MPIL showed an increasing phase starting two days after the first observation and continued until almost the end of the study period in the 0–1.8 Mm height range (Table 2). Above 1.8 Mm, the increasing phase started 2.5 days or even later from the moment of the first observation. In NLFFF and NF2 extrapolation models, the increasing phase of the MPIL started about two days after, on 2017 March 29 00:00:00, at all atmospheric heights. The increasing phase continued until close to the end of the study period. At heights ranging from 0 to 1.8 Mm, the MPIL crossed the threshold level of 62 Mm both in the PF and LFFF models. However, in the NLFFF and NF2 estimations, the MPIL crossed the threshold at all investigated atmospheric heights. The four different extrapolations indicate that the MPIL exceeded the 62 Mm level, but the threshold level was found to be crossed later at higher altitudes (see Table 2).

4.2. Unsigned Magnetic Flux of the Polarity Inversion Line (R-value)

The unsigned magnetic flux as parameterized in the R metric, which aims to differentiate flaring from nonflaring active regions, was proposed by Schrijver (2007). R quantifies the amount of unsigned magnetic flux around the PIL in the photosphere. To convert R to Maxwell units, as suggested by Schrijver (2007), one can multiply by the area of the $2''$ pixel magnetogram. To identify the high-gradient PILs, either the positive or negative flux densities are required to exceed 150 Mx cm^{-2} (hence the name "weighted"), otherwise $R = 0$,

as seen in several cases during the evolution of that metric in Figure 4.

More magnetic free energy is potentially available to fuel a big flare, increasing the probability of a major solar eruption, as the value of R increases. Schrijver (2007) found that, when log $R >$ 5.0, then at least one major flare is expected within 24 hr. A ~20% increasing tendency was also identified in the evolution of R before reaching a maximum state. The increasing tendency of log R is calculated between the first moment of the increasing phase and the reference value. The investigated increasing tendency is when the log R parameter's value remains above zero until the reference time. Therefore, based on Table 3 and Figure 4, the following was found.

1. *AR11166.* The log R parameter increased more than 20% between 0 and 1.44 Mm based on the PF/LFFF extrapolation data from 36/24 hr before the flare, respectively (Figures 4(a)–(b)). Above a height of 1.44 Mm, the evolution of log R cannot be analyzed, as most of the values become practically zero. In contrast, the NLFFF and NF2 extrapolations showed this preeruptive behavior of log R at heights of 0–3.24 Mm. Based on the calculated PF and LFFF data, log R exceeded the threshold level 11 and 37 hr before the X1.5 flare, respectively, only in the photosphere. However, according to the NLFFF and NF2 extrapolations, log R reached the threshold level between 0 and 0.72 Mm. log R reached a value >5 just a few hours earlier before the flare at 0.36 and 0.72 Mm in the case of NLFFF and NF2 (see Table 3).

2. *AR12645.* Here, the log R parameter also increased more than 20% between 0 and 0.72 Mm based on the PF and LFFF extrapolation data. In the NLFFF and NF2 models, the 20% increasing trend of log R was found to be

Table 3
Summary of the $\log R$ Analysis for AR11166 and AR12645 Using PF, LFFF, NLFFF, and NF2 Data

Height (Mm)	$T_{\log R > 5}$ (hr)				Increasing Rate of $\log R$ (%)				$\log R$ at the Reference Time			
	PF	LFFF	NLFFF	NF2	PF	LFFF	NLFFF	NF2	PF	LFFF	NLFFF	NF2
						AR11166						
0	11	37	71	32	37.9	25.0	39.6	45.8	5.10	5.18	5.10	5.14
0.36	...	...	5	7	38.5	49.2	51.7	42.1	4.72	4.75	5.05	5.06
0.72	...	...	1	2	44.5	47.6	38.2	44.3	4.24	4.37	5.02	5.05
1.08	...	...	...	...	36.2	35.3	30.6	43.2	3.81	3.74	4.86	4.86
1.44	...	...	...	...	22.3	22.7	27.8	48.2	3.13	3.13	4.81	4.71
1.8	...	...	...	...	...	...	28.4	39.6	...	...	4.89	4.53
2.16	...	...	...	...	...	...	50.5	35.9	...	...	4.73	4.34
2.52	...	...	...	...	...	...	38.9	39.7	...	...	4.67	4.09
2.88	...	...	...	...	...	...	37.2	26.1	...	...	4.59	3.78
3.24	...	...	...	...	...	...	36.8	26.0	...	...	4.3	3.37
3.6	...	...	...	...	...	...	...	...	...	...	...	...
						AR12645						
0	...	...	...	...	32.9	35.8	32.9	30.3	4.7	4.8	4.8	4.5
0.36	...	...	...	...	47.8	46.2	30.1	54.9	4.2	4.4	4.4	4.3
0.72	...	...	...	...	32.9	29.5	32.2	48.3	3.8	3.8	4.6	4.2
1.08	...	...	...	...	...	...	42.5	38.7	...	...	4.2	4.0
1.44	...	...	...	...	...	...	38.1	43.1	...	...	4.1	3.8
1.8	...	...	...	...	...	...	41.3	41.7	...	...	4.0	3.3
2.16	...	...	...	...	...	...	...	...	...	...	...	...
2.52	...	...	...	...	...	...	...	...	...	...	...	...
2.88	...	...	...	...	...	...	...	...	...	...	...	...
3.24	...	...	...	...	...	...	...	...	...	...	...	...
3.6	...	...	...	...	...	...	...	...	...	...	...	...

Note. The first column presents the investigated heights, and the subsequent four columns detail the number of hours $T_{\log R}$ earlier that $\log R$ exceeded the threshold value at various atmospheric heights before the reference time. The next four columns indicate the rate of increase of $\log R$ before the reference times at the corresponding heights. The last four columns display the actual values of $\log R$ at the reference time.

between 0 and 1.8 Mm (see Table 3). However, according to all four extrapolation models, $\log R$ remained below 5, which also suggests that no major eruption would be expected.

4.3. Effective Connected Magnetic Field (B_{eff})

Georgoulis & Rust (2007) developed a predictor, namely the effective connected magnetic field (B_{eff}). This parameter appears to be capable of discerning a flaring region from a nonflaring one, especially in the case of X- or M-class flares. B_{eff} provides information on the sum of all the magnetic flux connections of an active region, with each line corresponding to a connection of length L and net magnetic flux Φ weighted by their squared distance to obtain a value in magnetic field units. This metric is expressed as

$$B_{\rm eff} = \sum_{i=1}^{m} \sum_{j=1}^{l} \frac{\Phi_{ij}}{L_{ij}^2}. \qquad (2)$$

The parameter Φ_{ij} corresponds to the net magnetic flux associated with the connection (ij) in an active region, and L_{ij} is the distance separating the two ends of this connection, assumed to be the flux-weighted centroids of the magnetic flux partitions in the photosphere.

An advantage of this metric is that it is quite insensitive to spatial resolution; even with a low-resolution magnetogram, the measure of B_{eff} of an active region is not affected. Using this metric, it was found that X-/M-class flares could not occur in the next 12 hr when $B_{eff} < 750/200$ G, while they could when

$B_{eff} > 2100/1600$ G. However, even if we can determine some ranges where we know that an active region will or will not produce an X-class flare, there is still a range (750 G $< B_{eff}$ < 1600 G) where the method's output regarding the occurrence of a major flare is not binary (i.e., yes or no) but is still probabilistic. Therefore, here, we considered the condition B_{eff} > 750 G as a threshold level, which still indicates that a larger energetic flare (above M5-class flare) is probable. The outcome of this analysis is shown in Figure 5 and summarized in Table 4.

1. *AR11166.* The derived B_{eff} from the PF, LFFF, NLFFF, and NF2 models exhibited about a three-day long increasing phase before the X1.5 flare, as shown in Figures 5(a)–(d). In the case of PF and LFFF extrapolations, this parameter was above the 750 G threshold level a few hours before the X1.5 flare, between the photosphere and 0.36 Mm (see Table 4). Meanwhile, the NLFFF and NF2 data showed that B_{eff} exceeded the threshold level at higher altitudes. For the NLFFF model, B_{eff} was larger than 750 G a few hours earlier before the flare in the height range of 0–1.4 Mm. Notably, in the NF2 approximation, the proxy reached and remained above the 750 G threshold before the X1.5 flare, between 0 and 1.8 Mm. The threshold level was exceeded approximately 12 hr before the flare between 0 and 0.36 Mm.

2. *AR12645.* Based on all four extrapolations, B_{eff} exhibits an increasing phase between approximately 45 and 100 hr. After around 100 hr, B_{eff} stopped increasing and remained constant, albeit with significant fluctuations
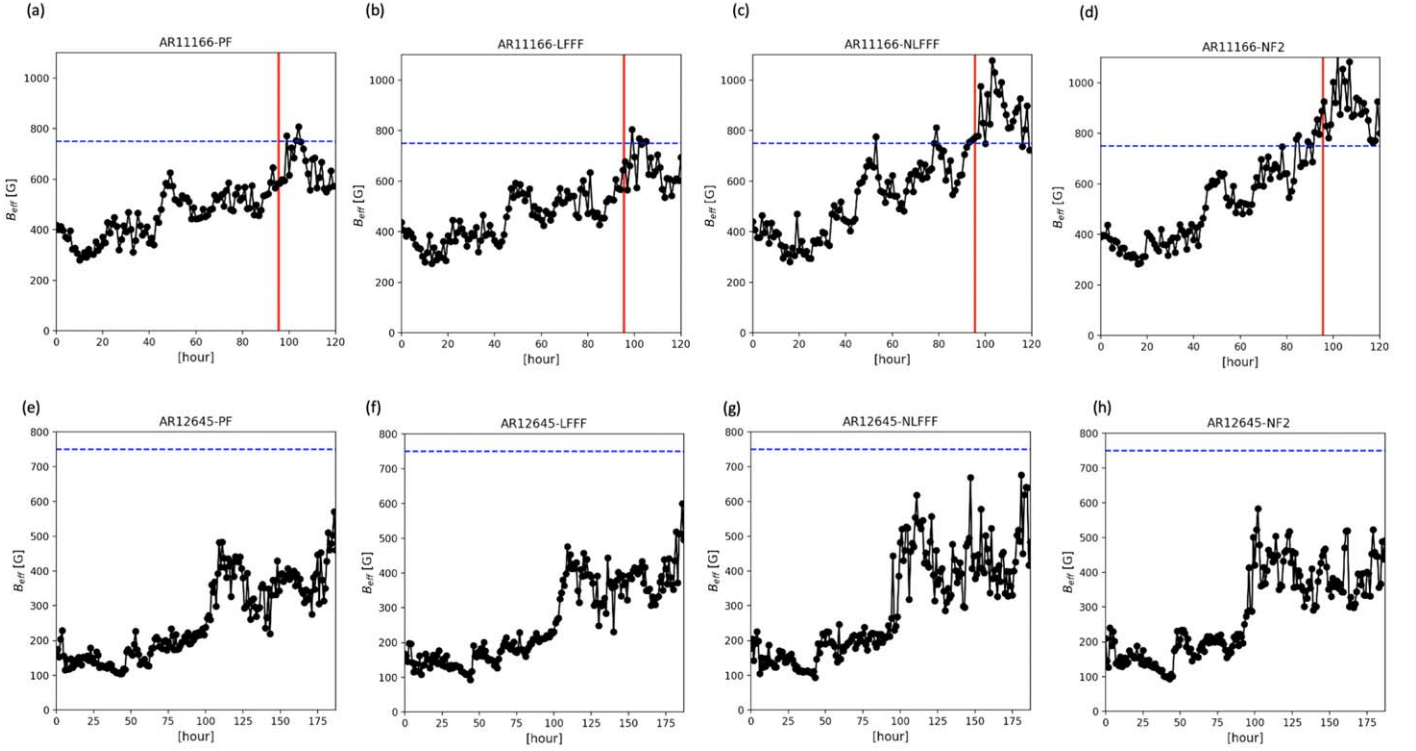
Figure 5. Panels (a)–(d) refer to the evolution of the B_{eff} parameter at 1.44 Mm above the solar surface based on the PF, LFFF, NLFFF, and NF2 extrapolations, respectively, in the case of AR11166. The red vertical lines represent the onset time of the X1.5 flare. Panels (e)–(h) refer to the case of nonflaring AR12645.

Table 4
Summary of the B_{eff} Analysis for AR11166 and AR12645 Using PF, LFFF, NLFFF, and NF2 Extrapolations. The Format Is Analogous to Table 2

Height (Mm)	$T_{\mathrm{Beff}>750G}$ (hr)				B_{eff} at the Reference Time			
	PF	LFFF	NLFFF	NF2	PF	LFFF	NLFFF	NF2
				AR11166				
0	6	6	7	15	1211.9	1163.1	1188.1	1335.1
0.36	4	4	6	12	854.0	843.3	992.8	1405.7
0.72	...	...	6	5	735.7	732.4	895.4	1050.0
1.08	...	...	5	5	641.3	654.4	811.8	847.1
1.44	...	...	3	4	583.9	677.7	778.3	925.7
1.8	...	...	...	2	553.5	566.3	720.9	780.1
2.16	...	...	...	...	549.7	563.8	655.3	721.4
2.52	...	...	...	...	515.8	514.4	622.5	633.3
2.88	...	...	...	...	440.0	444.5	537.9	704.7
3.24	...	...	...	...	388.2	393.5	578.9	640.8
3.6	...	...	...	...	367.1	465.1	588.0	627.7
				AR12645				
0	...	...	...	...	624.1	667.3	633.5	504.4
0.36	...	...	...	...	622.0	637.6	582.5	595.3
0.72	...	...	...	...	507.1	446.4	584.1	447.1
1.08	...	...	...	...	565.2	510.4	594.4	489.9
1.44	...	...	...	...	460.7	495.4	483.5	491.7
1.8	...	...	...	...	514.7	470.6	429.5	435.6
2.16	...	...	...	...	430.6	429.9	385.3	390.0
2.52	...	...	...	...	358.8	283.3	480.2	392.4
2.88	...	...	...	...	309.5	316.9	382.4	261.6
3.24	...	...	...	...	350.9	245.3	284.6	239.1
3.6	...	...	...	...	228.2	241.9	269.8	253.4

in all four extrapolation scenarios, as illustrated in Figures 5(e)–(h). B_{eff} did not surpass the threshold level of 750 G, indicating that this active region was likely incapable of generating a powerful solar flare.

4.4. The Gradient-weighted Length of Strong-field PILs (WL$_{SG}$)

The purpose of the gradient-weighted integral length of the neutral line (WL$_{SG}$) is to indirectly quantify the free magnetic
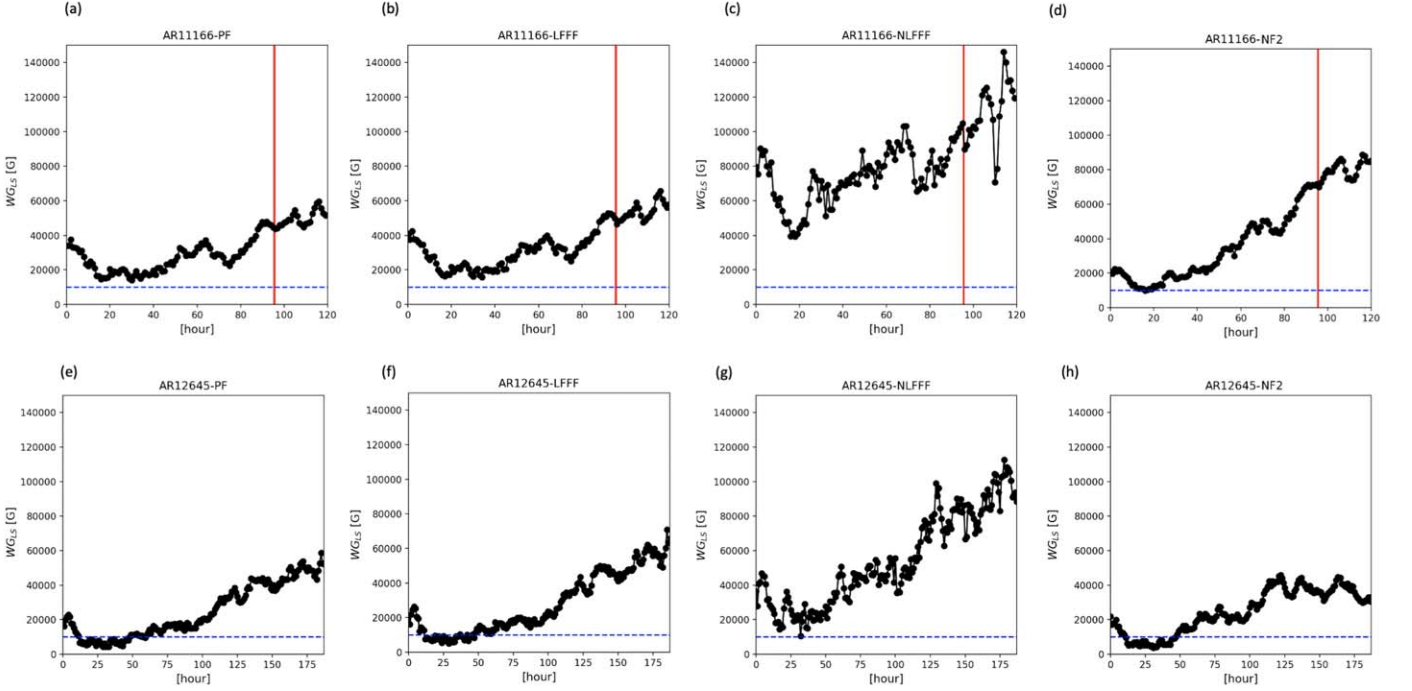
Figure 6. Panels (a)–(d) refer to the evolution of the WG_{LS} parameter at 0.72 Mm above the solar surface based on the PF, LFFF, NLFFF, and NF2, respectively, in the case of AR11166. The red vertical lines represent the onset time of the X1.5 flare. Panels (e)–(h) refer to the case of nonflaring AR12645.

energy of an active region. This proxy takes the strong-field intervals of the PIL to be those on which the horizontal field computed from the vertical field component of the magnetogram is >150 G. This parameter is expressed as

$$\mathrm{WL}_{SG} = \int |\nabla B_z| \, dl, \qquad (3)$$

where $|\nabla B_z|$ is the horizontal gradient of the vertical magnetic field and WL_{SG} has units of G. The probability of a major solar eruption decreases as WL_{SG} decreases, and it approaches zero when WL_{SG} falls below approximately 10^4 G. Falconer et al. (2012) concluded that a major solar eruption could be expected with 75% possibility in the next 24 hr prediction window if $\mathrm{WL}_{SG} > 10^4$ G.

Based on Figure 6 and Table 5, we report the following main findings.

1. *AR11166.* The WL_{SG} proxy starts to increase about 1.5 days after the first observation of the active region and continues to increase even after the X1.5 flare throughout the entire 0–3.16 Mm height range in the case of PF and LFFF extrapolations. However, based on NLFFF and NF2 data, the increasing period of WL_{SG} started about a day later from the first moment of the time series at every analyzed atmospheric height. The WL_{SG} remained above the 10^4 G threshold level for several days before the flare eruption occurred at a height of 0–1.8 Mm in both the PF and LFFF extrapolation models. The preeruptive condition of the proxy was also satisfied days before the flare in the NLFFF and NF2 models, from the solar surface up to 3.6 Mm.

2. *AR12645.* WL_{SG} showed an increasing period after two days from the first moment between 0 and 2.16 Mm, based on the PF and LFFF data (see Figures 6(e)–(f)). Above 2.16 Mm, the WL_{SG} started to increase about four

days later from the first observation. In the case of the NLFFF and NF2 models, the WL_{SG} started to increase about 1.5–2 days after the first moment of the time series between 0 and 3.6 Mm. However, following approximately two days of increasing activity, the WL_{SG} attained its peak value and demonstrated a pattern of half-day decrease followed by half-day increase above 2.16 Mm for the entirety of the study period in the NLFFF scenario. According to the NF2 construction of the magnetic field structure of this active region, a comparable pattern of WL_{SG} behavior can be observed after a three-day increasing period, originating from the photosphere and extending upwards (see Figure 6(h)). Furthermore, WL_{SG} remained above the 10^4 G threshold level for more than 24 hr before the moment of the last observation occurred between 0 and 2.16 Mm in both the PF and LFFF extrapolations. In the case of the NLFFF and NF2 extrapolation models, the WL_{SG} showed a preflare condition from the photosphere up to 3.6 Mm.

We note that the trend of WL_{SG} evolution is similar in the four extrapolation cases. However, the magnitude of the WL_{SG} parameter is quite different in the case of NLFFF and NF2, whereas in the other parameters it evolves similarly. The other applied parameters, here, are calculated more straightforwardly. To calculate the WL_{SG} parameter, a two-level estimation process is needed. (i) As a first step, we get an estimated value for the WL_{SG}. (ii) Next, for the final value of the WL_{SG} parameter, we need to search the neighboring pixels for nonzero values in the MPIL region; once the increments are correctly detected, we interpolated at midpoint. Finally, the WL_{SG} parameter is derived.

The application of the WL_{SG} even further supports that PF ($\alpha = 0$) and LFFF ($0 < \alpha < 1$) extrapolation provide a similar result, as the α is close to zero and fixed through a 3D volume during the LFFF approach, whereas, during the NLFFF

9

Table 5
Summary of the WG$_{LS}$ Analysis for AR11166 and AR12645 Using PF, LFFF, NLFFF, and NF2 Data

Height (Mm)	$T_{\mathrm{WG_{LS}>10^4G}}$ (hr)				WG$_{LS}$ at the Reference Time			
	PF	LFFF	NLFFF	NF2	PF	LFFF	NLFFF	NF2
				AR11166				
0	79	77	77	79	142676.9	109872.1	112576.2	95118.0
0.36	62	62	79	79	65280.0	74920.1	90100.1	80178.9
0.72	66	62	78	80	43739.4	46610.3	89871.1	69964.4
1.08	54	54	78	76	31456.1	32637.2	108925.9	62994.3
1.44	46	46	79	70	22646.1	23202.8	121010.9	56491.3
1.8	43	43	77	58	16044.0	16360.5	116167.9	51040.2
2.16	4	4	64	57	11964.5	12045.7	110714.5	45122.9
2.52	...	...	73	52	8671.8	8742.4	98007.0	40327.7
2.88	...	...	64	46	6947.7	6937.9	89193.4	35653.3
3.24	...	...	64	38	5381.9	5395.2	75604.3	31119.7
3.6	...	...	64	32	4063.9	4969.6	70597.8	27388.4
				AR12645				
0	154	154	159	156	170559.4	174969.8	166753.3	52731.1
0.36	158	159	163	156	91960.4	120198.1	114901.8	39026.3
0.72	140	140	155	141	51839.0	63592.6	88399.5	30472.1
1.08	93	123	160	138	32676.9	35929.7	99101.6	25730.5
1.44	85	85	164	127	23416.0	24505.4	90669.5	23926.0
1.8	82	82	164	97	16573.5	18929.4	82946.1	20848.3
2.16	45	45	164	88	14186.8	13748.0	75144.0	17946.2
2.52	5	5	164	88	11092.2	10204.6	59909.7	14766.9
2.88	...	...	160	87	8854.5	8680.6	51582.8	13503.2
3.24	...	...	147	82	6677.4	6330.5	43255.8	12159.3
3.6	...	...	145	28	4954.4	5657.2	37574.5	10630.7

extrapolation, the α changes through a 3D volume, as in the case of NF2. However, the NF2 additionally also learns from the previously extrapolated data.

4.5. Ising Energy (E_{Ising})

Ahmed et al. (2010) have proposed that the Ising energy (E_{Ising}) of a group of magnetic elements that interact with each other and are depicted by image pixels can be computed using the equation

$$E_{\mathrm{Ising}} = \sum_{ij} \frac{S_i S_j}{d^2}, \qquad (4)$$

where S_i (S_j) is equal with $+1$ (-1) based on the positive (negative) magnetic polarity of each pair of pixels, and then divided by the square distance (d) between the opposing polarity pixels. Hence, it can be inferred that a large number of opposite polarity pixels that are closely situated, such as those along PILs, would have a greater impact on E_{Ising} than those that are widely spaced apart. The Ising model is a fundamental model for ferromagnetism, explaining how the transition of materials from nonmagnetic to magnetic states takes place (Peierls 1936).

In order to obtain accurate results, the magnetograms are first corrected for position angle, and then smoothed using a five-pixel running average along both the x- and y-axis. Additionally, pixels with weak magnetic field strengths are disregarded by applying a threshold of 100 G. Ahmed et al. (2010) found that, if E_{Ising} is larger than 10,000 pixels^{-2}, then an active region has a high probability of producing a large flare. The analysis of this parameter shows this via Figure 7 and Table 6.

1. *AR11166*. The increasing phase of the E_{Ising} time series started approximately 1.5 days after the first data point between 0 and 3.6 Mm for the PF, LFFF, NLFFF, and NF2 models. These increasing phases stopped just a few hours after the X1.5 flare at all investigated heights. E_{Ising} remained larger than the 10,000 pixels^{-2} threshold value from the beginning to the solar flare, from the photosphere to 3.6 Mm, for all four extrapolation datasets.
2. *AR12645*. The proxy started to increase about two days later from the first observation until the end of the time series between 0 and 3.6 Mm, based on the four extrapolation data. Similar to AR11166, E_{Ising} was well above the threshold level up to 3.6 Mm for all four extrapolations. However, the threshold level was crossed later as altitude increased above 1.8, 2.16, and 2.52 Mm based on the PF, LFFF, and NF2 models (see Table 6). In the case of the NLFFF magnetic field structure, the threshold was reached almost at the same time from the solar surface up to 3.6 Mm.

4.6. Unique Oscillatory Behavior Pattern of the Magnetic Helicity Flux

Magnetic helicity is a fundamental property of magnetic fields, and it may measure the degree of twisting and linkage of magnetic field lines. Soós et al. (2022) found a relationship between the flaring activities and the unique oscillatory behavior pattern of the emergence (EM), shearing (SH), and total (T) magnetic helicity flux components. Korsós et al. (2022) further analyzed these unique oscillatory behaviors of the magnetic helicity components. It was found that the largest identified photospheric periods of the EM, SH, and T helicity fluxes remain the most prominent. These periods are common and persist at least up to 1 Mm above the
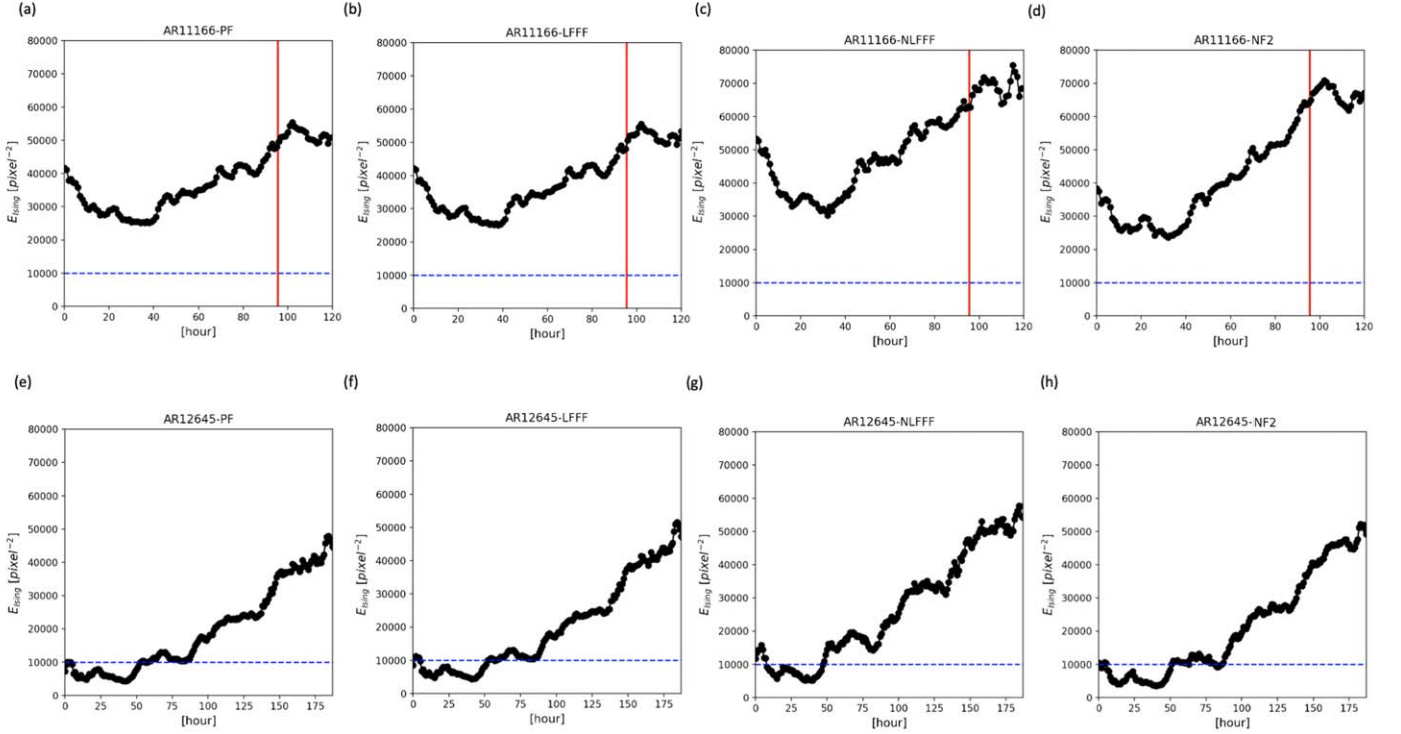
Figure 7. Panels (a)–(d) refer to the evolution of the $E_{\rm Ising}$ parameter at 1.8 Mm above the solar surface based on the PF, LFFF, NLFFF, and NF2 extrapolation, respectively, for AR11166. The red vertical lines represent the onset time of the X1.5. Panels (e)–(h) are for the nonflaring AR12645.

Table 6
Similar to Tables 2–5, but Providing Information about the Analysis of the $E_{\rm Ising}$ for Both AR11166 and AR12645 Using PF, LFFF, NLFFF, and NF2 Data

Height (Mm)	$T_{E_{\rm Ising} > 10^4}$ (hr)				$E_{\rm Ising}$ at the Reference Time			
	PF	LFFF	NLFFF	NF2	PF	LFFF	NLFFF	NF2
				AR11166				
0	96	96	96	96	55593.6	54722.9	55649.2	56209.2
0.36	96	96	96	96	54239.1	54008.3	57602.1	59171.6
0.72	96	96	96	96	52890.9	53132.2	59575.7	61460.4
1.08	96	96	96	96	51963.7	52264.3	61297.7	63433.1
1.44	96	96	96	96	50940.0	51677.3	63311.3	64586.6
1.8	96	96	96	96	49559.7	50623.5	62800.3	64901.7
2.16	96	96	96	96	48081.0	49042.9	63813.8	64685.4
2.52	96	96	96	96	47129.0	48397.5	64282.9	64008.1
2.88	96	96	96	96	46145.2	47523.7	65976.9	63411.5
3.24	96	96	96	96	45540.7	47242.1	64891.1	62596.7
3.6	96	96	96	96	45201.6	47227.2	64807.0	61729.5
				AR12645				
0	139	139	139	137	76221.2	81840.1	75484.9	52857.6
0.36	138	138	138	137	61616.1	63501.5	66336.8	52557.9
0.72	137	137	138	136	55483.1	56959.4	55575.9	51944.8
1.08	135	136	139	136	51982.0	54003.6	59341.1	50890.7
1.44	135	135	139	136	48391.2	50635.1	56853.0	50088.0
1.8	128	134	139	136	44677.2	47291.5	54162.1	49160.8
2.16	126	126	139	135	41595.3	44651.8	52490.5	49004.1
2.52	102	111	139	100	38324.9	41764.1	50220.2	49329.3
2.88	101	101	139	100	35545.3	39348.0	48196.5	49588.5
3.24	102	102	139	100	33178.8	37213.1	45724.6	49838.5
3.6	102	102	139	100	30456.2	30176.5	43241.9	49818.7

photosphere, days before a flare event. This was concluded as the horizontal and the vertical helicity flux components become a coupled oscillatory system in the LSA before a major solar eruption. Such oscillations in helicity could have implications for the buildup and release of magnetic energy in the solar atmosphere, leading to events such as a major solar eruption.
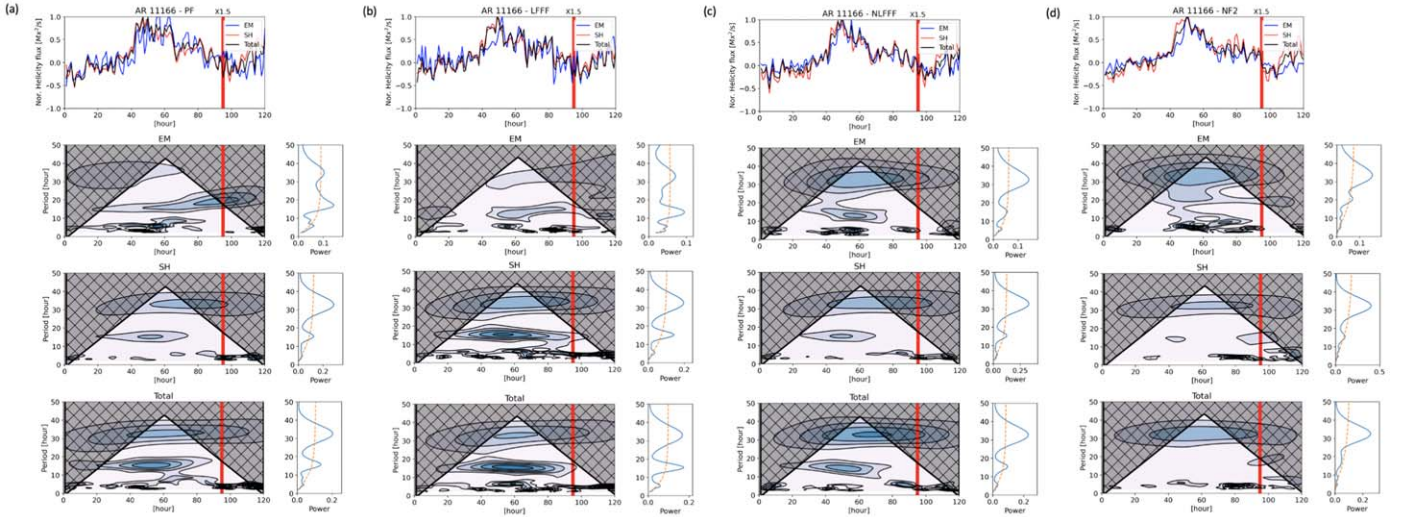
Figure 8. Panels (a)–(d) refer to the wavelet analyses of the EM, SH, and T magnetic helicity flux parameter in the photosphere using PF, LFFF, NLFFF, and NF2 extrapolations, respectively, for AR11166. The red vertical lines represent the onset time of the X1.5 flare. The top panels show time series of the normalized emergence EM (blue line), shearing SH (red line), and total T (black line) helicity fluxes. The second, third, and fourth rows are the wavelet power spectrum of the EM, SH, and T. The x-axis of each wavelet power spectrum denotes the evolution of the data, and the y-axis is the period. On the wavelet power spectrum plots, the hatched black lines bound the cone of influence. The contour encloses regions that are greater than the 1σ confidence level for a red-noise process. The contour intervals are differences in rising between contour lines. The plots to the right of each wavelet power spectrum are the corresponding global wavelet spectra with power averaged over time. The black dashed lines mark the 1σ confidence level in the global wavelet spectra analyses.

Table 7
Summary Information: the First Column Presents the Investigated Heights of AR11166 in the Case of Using PF, LFFF, NLFFF, and NF2 Models

Height (Mm)	EM Largest Period (hr)				SH Largest Period (hr)				T Largest Period (hr)			
	PF	LFFF	NLFFF	NF2	PF	LFFF	NLFFF	NF2	PF	LFFF	NLFFF	NF2
						AR11166						
0	34.2	34.2	33.1	33.1	33.1	33.1	33.1	33.1	33.1	33.1	33.1	31.9
0.36	33.7	33.9	31.9	31.9	33.1	33.1	33.1	31.9	31.9	33.1	33.1	31.9
0.72	34.4	34.2	30.8	31.9	31.9	33.1	33.1	31.9	32.3	33.1	33.1	30.8
1.08	35.7	33.7	30.4	31.9	32.8	31.9	33.1	33.1	32.8	31.9	31.9	30.8
1.44	35.7	34.4	...	...	32.8	31.9	...	...	32.8	30.8	...	...
1.8	35.4	34.2	...	...	32.9	31.9	...	...	31.8	30.8	...	...
2.16	35.7	35.4	...	...	32.1	31.9	...	...	31.9	30.8	...	...
2.52	...	...	...	...	...	...	...	...	...	...	...	...
2.88	...	...	...	...	...	...	...	...	...	...	...	...
3.24	...	...	...	...	...	...	...	...	...	...	...	...
3.6	...	...	...	...	...	...	...	...	...	...	...	...

Note. The last 12 columns display the detected largest period of the EM, SH, and T helicity flux components at the corresponding atmospheric heights in the case of EM, SH, and T.

1. *AR11166*. The time series of the EM, SH, and T are similar in the case of PF, LFFF, NLFFF, and NF2 extrapolations (see Figures 8(a)–(d)). Furthermore, the evolution of the three helicity flux components vary similarly as a function of height in all the extrapolation cases. The measured largest and common period of the three helicity flux components is 31–34 hr, determined via the wavelet analyses based on the four extrapolations data (see Figures 8(a)–(d)). This period remains the largest and the common one from the photosphere to 2.16 Mm for the case of PF and LFFF modeling (see Figures 10(a)–(b) and Table 7). However, this largest and most common period was identified between 0 and 1.08 Mm both in NLFFF and NF2 extrapolation cases (see Figures 10(c)–(d) and Table 7). The local maxima of

the common period can be measured 5/12 hr earlier at 0.36/0.72 Mm when compared to the solar surface in the case of PF/LFFF magnetic structures of the active region. When investigating the NLFFF/NF2 data, the local maximum could be measured 17/7 hr earlier at 1.08 Mm (see Table 7 and Figure 10).

2. *AR12645*. Similar to the flaring active region case, the time series of the EM, SH, and T are basically similar in the cases of PF, LFFF, NLFFF, and NF2 magnetic field constructions (see Figures 9(a)–(d)). The evolution of the three helicity flux components also vary as a function of height in all four extrapolation cases. However, the largest period of the EM is different compared to the largest period of SH and T based on the four extrapolation data, which was also found in the case of nonflaring active regions via Korsós et al. (2022).
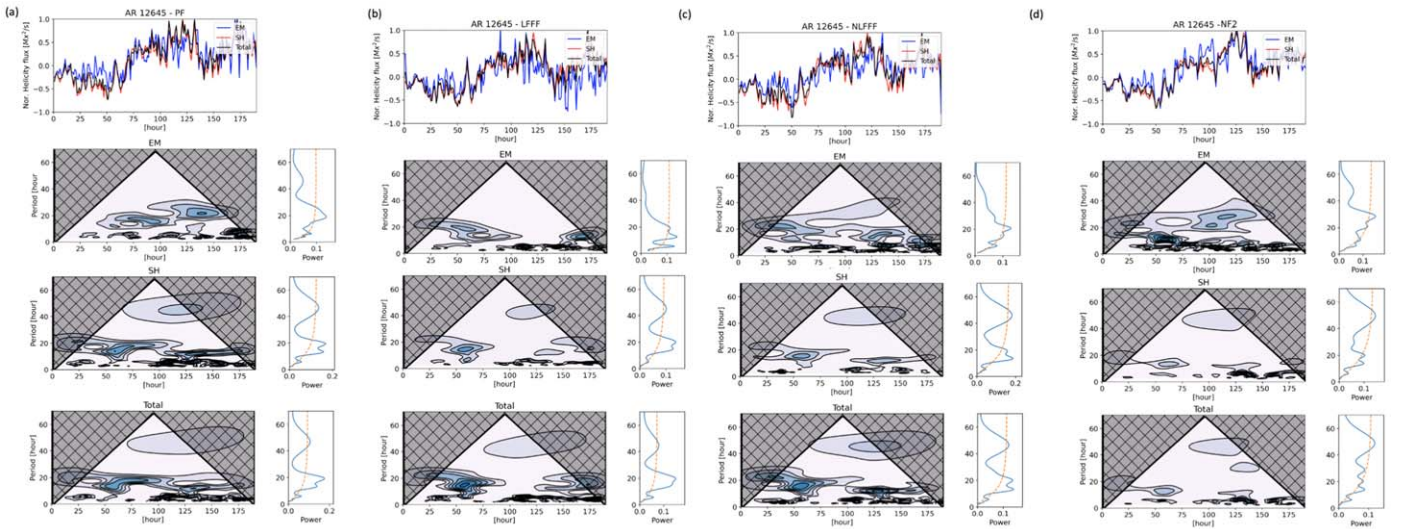
Figure 9. Panels (a)–(d) refer to the wavelet analyses of the EM, SH, and T magnetic helicity flux parameter in the photosphere based on the PF, LFFF, NLFFF, and NF2 models, respectively, for AR12645.

5. Discussion and Conclusion

Most solar eruption prediction methods apply different photospheric observations (e.g., continuum, magnetic field, and Doppler data) of solar active regions or upper solar atmospheric measurements (e.g., extreme ultraviolet data) to improve the flare–CME prediction accuracy (see, e.g., Barnes et al. 2016; Florios et al. 2018; Leka et al. 2019; Georgoulis et al. 2021; Sun et al. 2023, and references therein). Nevertheless, detailed information on measuring and the consequent modeling of the 3D magnetic field structure of an active region would be important to obtain a more accurate insight into the preflare–CME evolution locally in the LSA, where these solar eruptions form and manifest (e.g., Kuridze et al. 2019; Erdélyi et al. 2022). Unfortunately, direct routine and continuous observations of the 3D magnetic field in the LSA (above the photosphere up into the top of the chromosphere) are currently not yet available (Vissers et al. 2022). However, we have available regular high-cadence measurements of the LOS components and full magnetic field vector observations in the photosphere. These photospheric magnetic field measurements are routinely used as input data to construct the 3D lower solar atmospheric magnetic field structure of active regions.

To investigate the applicability and importance of different 3D extrapolation approaches for flare prediction, we first employed the PF, LFFF, and NLFFF extrapolation models, as proposed by Wiegelmann et al. (2012). Additionally, we utilized a physics-based neural network approach for coronal field extrapolation that integrates observational data and the physical NLFFF model by Jarolim et al. (2023).

We conducted an analysis of the evolution of the 3D magnetic field structure of two active regions with rather different flare activity levels. The first active region (AR11166) exhibited flaring behavior and had a notable X1.5 flare event on 2011 March 9 at 23:13 UTC. The second active region (AR12645) did not produce any intense flares during its observation period. Both active regions had complex δ-spot magnetic configurations. Based on the calculated magnetic free energy, E_{free}, of the two active regions, it can be concluded that AR11166 possesses approximately an order of magnitude more available free (i.e., nonpotential) energy than AR12645.

To analyze the evolution of the 3D magnetic field structure in the LSA of these two active regions, we selected six promising prediction parameters and analyzed the two active regions during the disk passage in the LSA. Five out of the six selected parameters were based on the FLARECAST project proposed by Georgoulis et al. (2021): the MPIL (Falconer et al. 2003; Mason & Hoeksema 2010), the unsigned magnetic flux of the polarity inversion line, $\log R$ (Schrijver 2007), the effective connected magnetic field, B_{eff} (Georgoulis & Rust 2007), the gradient-weighted length of strong-field PILs, WL$_{\text{SG}}$ (Falconer et al. 2012), and the Ising energy, E_{Ising} (Ahmed et al. 2010). Last but not least, another widely used parameter is the magnetic helicity flux (Korsós et al. 2022; Soós et al. 2022; Liu et al. 2023).

Based on our analyses, we found the following.

1. *AR11166.* For this flare-productive active region, the MPIL, B_{eff}, WL$_{\text{SG}}$, E_{Ising}, and magnetic helicity flux fulfill their respective preeruptive conditions not only within the photosphere but also at higher altitudes, as derived on the basis of the four extrapolation models. $\log R$, however, shows its preeruptive conditions above the photosphere solely in the case of the NLFFF and NF2 approaches. In contrast, within the framework of the PF and LFFF models, $\log R$ shows preeruptive conditions only in the photosphere. The applied proxies satisfy their preeruptive conditions at greater heights in the context of NLFFF and NF2 data, in contrast to PF and LFFF (refer to Tables 2–6), while it is opposite in the case of studying the unique oscillatory behavior pattern of the magnetic helicity flux (see, e.g., Figure 10).

2. *AR12645.* In this case, $\log R$, B_{eff}, and the distinctive oscillatory behavior pattern of the magnetic helicity flux did not reach their individual threshold values and/or satisfy their own preflare behavior based on the four magnetic field extrapolation values. Conversely, the remaining three parameters demonstrated these conditions within the photosphere, extending to certain lower heights within the solar atmosphere. Much like the flaring active region, the maximum atmospheric heights, where the MPIL and WL$_{\text{SG}}$ surpass their individual threshold values, coincide across the PF and LFFF data. Notably,
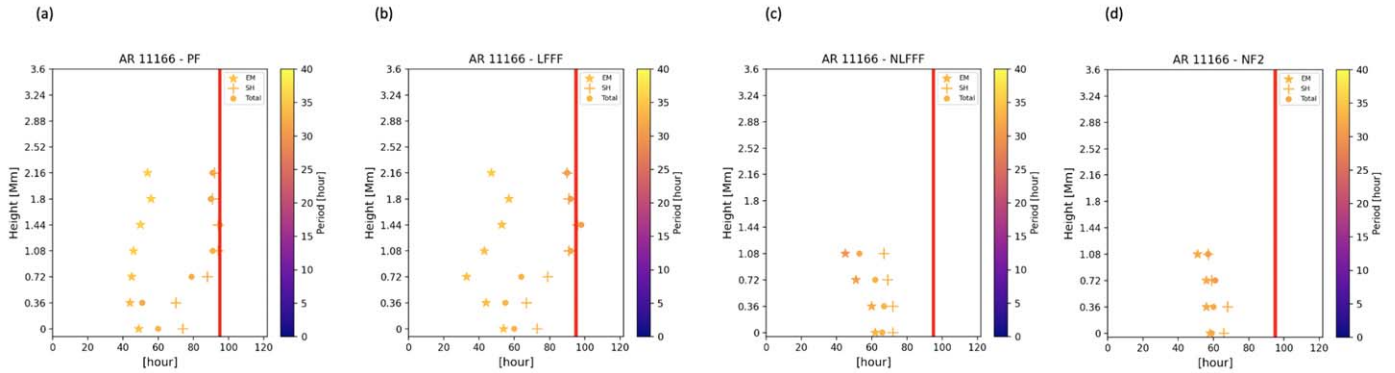
Figure 10. Panels (a)–(d) refer to the local maximum peaks of the identified largest periods of EM, SH, and T magnetic helicity flux parameters at different heights using PF, LFFF, NLFFF, and NF2 extrapolations, respectively, in the case of AR11166. The red vertical lines represent the onset time of the X1.5 flare.

the maximum heights of MPIL and WL_{SG} exceed those observed in the case of AR11166 under PF and LFFF data. Meanwhile, the WL_{SG} predictor satisfies its own preeruptive condition at all altitudes within the context of the NLFFF and NF2 data. Similarly, akin to the situation in AR11166, the E_{Ising} parameter consistently remains above the threshold at every studied atmospheric height across all four magnetic field extrapolation values.

3. In general, when considering the four types of magnetic field extrapolations, the evolution of the applied morphological parameters exhibits similarity throughout the investigated time period. However, the magnitude of the WL_{SG} parameter is quite different in the case of NLFFF and NF2, whereas, in the other parameters, it evolves similarly. This could relate to the fact that the other applied parameters are calculated more straightforwardly, while for the WL_{SG} we need to employ two-level estimation processes (for more details, see the end of Section 4.4).

4. For each parameter, the identified maximum heights in the LSA are the same based on PF and LFFF analyses. This pattern is also observed in the case of NLFFF and NF2 approximations, except for the maximum height of NF2, which surpasses that of NLFFF specifically in the context of B_{eff} (see Table 1).

It was shown that the derived morphological/proxy parameters were similarly developed based on the PF, LFFF, NLFFF, and NF2 extrapolation values. However, for the purpose of flare prediction, in practice, one requires a relatively quick extrapolation method. Based on the aforementioned results, we can indirectly deduce that the PF, LFFF, and NF2 methods are viable options due to their required computation times. The computation time of the 3D magnetic field by NF2 is comparable with LFFF and PF extrapolations. The 3D magnetic field computation time for (i) NF2 is 60–100 minutes/observation using four NVIDIA V100 GPUs for computation; (ii) LFFF is 40–70 minutes/observation; and (iii) PF is 20–30 minutes/observation depending on the size of the active region NVIDIA CUDA with 8 CPU. However, the computation of NLFFF could be as long as from several hours up to 24 hr/observation NVIDIA CUDA with 8 CPU, which is not really suitable in the context of live space weather forecasting. If one would like to use a more accurate assumption, then the NF2 would be the most recommended one (Jarolim et al. 2023).

Drawing from these magnetically complex active regions, we can also infer that there is merit in broadening the utilization of a combination of distinct prediction parameters in the LSA. This expansion holds the potential for enhancing the forecast accuracy of significant solar eruptions. For example, a certain maximum atmospheric height, where the predictors satisfy their own preeruptive conditions, would provide more accurate information on whether a flare is accompanied by a CME or not.

In the future, the PF, LFFF, and NF2 extrapolation methods should be applied to a larger number and variety of active regions to build statistics. Our goal is to further investigate and clarify the strengths and weaknesses of various approaches for predicting solar flares, based on LSA conditions. Based on the current findings, NF2 is preferred over NLFFF, since both give similar results, but NF2 offers considerable improvement in computational efficiency, rendering it more appropriate for prediction purposes.

ORCID iDs

Marianna B. Korsós ⓘ https://orcid.org/0000-0002-0049-4798
Robert Jarolim ⓘ https://orcid.org/0000-0002-9309-2981
Robertus Erdélyi ⓘ https://orcid.org/0000-0003-3439-4127

Astrid M. Veronig ⓘ https://orcid.org/0000-0003-2073-002X
Huw Morgan ⓘ https://orcid.org/0000-0002-6547-5838
Francesca Zuccarello ⓘ https://orcid.org/0000-0003-1853-2550

References

Ahmed, O. W., Qahwaji, R., Colak, T., Dudok De Wit, T., & Ipson, S. 2010, Vis Comput, 26, 385

Barnes, G., Leka, K. D., Schrijver, C. J., et al. 2016, ApJ, 829, 89

Bobra, M. G., Sun, X., Hoeksema, J. T., et al. 2014, SoPh, 289, 3549

Erdélyi, R., Korsós, M. B., Huang, X., et al. 2022, JSWSC, 12, 2

Falconer, D. A., Moore, R. L., Barghouty, A. F., & Khazanov, I. 2012, ApJ, 757, 32

Falconer, D. A., Moore, R. L., & Gary, G. A. 2003, JGRA, 108, 1380

Fletcher, L., Dennis, B. R., Hudson, H. S., et al. 2011, SSRv, 159, 19

Florios, K., Kontogiannis, I., Park, S.-H., et al. 2018, SoPh, 293, 28

Georgoulis, M. K., Bloomfield, D. S., Piana, M., et al. 2021, JSWSC, 11, 39

Georgoulis, M. K., Nindos, A., & Zhang, H. 2019, RSPTA, 377, 20180094

Georgoulis, M. K., & Rust, D. M. 2007, ApJL, 661, L109

Green, L. M., Török, T., Vršnak, B., Manchester, W., & Veronig, A. 2018, SSRv, 214, 46

Jarolim, R., Thalmann, J. K., Veronig, A. M., & Podladchikova, T. 2023, NatAs, 7, 1171

Kim, T., Park, E., Lee, H., et al. 2019, NatAs, 3, 397

Korsós, M. B., Chatterjee, P., & Erdélyi, R. 2018, ApJ, 857, 103

Korsós, M. B., & Erdélyi, R. 2016, ApJ, 823, 153

Korsós, M. B., Erdélyi, R., Huang, X., & Morgan, H. 2022, ApJ, 933, 66

Korsós, M. B., Georgoulis, M. K., Gyenge, N., et al. 2020, ApJ, 896, 119

Kuridze, D., Mathioudakis, M., Morgan, H., et al. 2019, ApJ, 874, 126

Leka, K. D., Dissauer, K., Barnes, G., & Wagner, E. L. 2023, ApJ, 942, 84

Leka, K. D., Park, S.-H., Kusano, K., et al. 2019, ApJS, 243, 36

Liokati, E., Nindos, A., & Liu, Y. 2022, A&A, 662, A6

Liu, J., & Huang, X. 2021, NatAs, 5, 108

Liu, Y., Welsch, B. T., Valori, G., et al. 2023, ApJ, 942, 27

Mason, J. P., & Hoeksema, J. T. 2010, ApJ, 723, 634

Peierls, R. 1936, PCPS, 32, 477

Raissi, M., Perdikaris, P., & Karniadakis, G. E. 2019, JCoPh, 378, 686

Sammis, I., Tang, F., & Zirin, H. 2000, ApJ, 540, 583

Schrijver, C. J. 2007, ApJL, 655, L117

Soós, S., Korsós, M. B., Morgan, H., & Erdélyi, R. 2022, ApJ, 925, 129

Sun, D., Huang, X., Zhao, Z., & Xu, L. 2023, ApJS, 266, 8

Toriumi, S., & Wang, H. 2019, LRSP, 16, 3

van Driel-Gesztelyi, L., & Green, L. M. 2015, LRSP, 12, 1

Vemareddy, P., & Wiegelmann, T. 2014, ApJ, 792, 40

Vissers, G. J. M., Danilovic, S., Zhu, X., et al. 2022, A&A, 662, A88

Wiegelmann, T., & Sakurai, T. 2021, LRSP, 18, 1

Wiegelmann, T., Thalmann, J. K., Inhester, B., et al. 2012, SoPh, 281, 37

Wiegelmann, T., Thalmann, J. K., & Solanki, S. K. 2014, A&ARv, 22, 78